Chapter 9 : *In vivo* Quantification of Carotid Plaque Strain

Finally, we present results from *in vivo* characterization of carotid plaque strain with diagnostic ultrasound via an externally applied transducer. First, the algorithms to generate the strain images and reduce the results are described. This includes an explanation of how the algorithms described in Chapters 3, 4, and 5 are applied as an integrated algorithm. Additionally, new features are covered, including the hierarchical framework for increasing motion tracking robustness. Finally, case studies of exemplar subjects are presented.

9.1 Hierarchical framework

9.1.1 Multi-level motion tracking

Multi-resolution motion tracking methods have long been established as the way to increase the speed and robustness of medical image registration [1, 2, 3, 4, 5, 6, 7, 8]. In general, a coarse-to-fine tracking scheme is applied by performing registration of the image pair at multiple resolutions. Results from registration at a coarser resolution level are used to initialize the registration problem at the next, finer resolution level. The lower resolution images are often subsampled, so motion tracking is faster. Even though multiple registration operations are performed at every level, including the finest level at the original image resolution, the overall motion tracking method is often quicker than a single non-hierarchical registration. By initializing the search close to the true displacements at finer levels, the solution space that must be examined in a more computationally taxing setting is greatly reduced. Also, local minima in

the solution associated with the high frequency content in the fine resolution images are avoided. This improves robustness of the algorithm.

Multi-resolution methods have also been applied to ultrasound strain imaging. Yeung et al. and Pellot-Barakat et al. have developed multilevel regularized, block-matching algorithm for tracking ultrasound speckle [9, 10]. In Yeung et al., coarser level images were not subsampled on the premise that high-frequency speckle information would be lost. Instead, the multi-resolution notion is applied by changing the matching-block size and the search region extent. Displacements are initially found with a large matching-block and wide search region and are transitioned to a small matching-block and confined search region. The large matching-blocks are not as sensitive to decorrelation noise. Smaller matching-blocks are not as affected by intra-block non-rigid motion and are capable of more precise displacements. Shi and Varghese discussed a multilevel where coarser levels were downsampled versions of the envelope image [11]. Instead of only using displacements at coarser levels to initialize the search region at finer levels, Bai et al., combined the cross-correlation results from window lengths at multiple levels to determine the displacements at the finest level [12]. Basarab et al. found that iterative application of multi-resolution initialization can improve results [13]. Chen et al. applied the multi-level approach to a quality-guided (seed propagation) algorithm [14].

Multi-resolution methods are particularly useful when imaging arteries, where there is motion discontinuity at the artery wall. Other block-matching motion tracking algorithms often propagate match-block search regions from prior displacements of high confidence [15, 13]. These restricted search regions reduce the detection of local minima in the similarity metric (peak-hopping errors). This continuity cannot be assumed when the artery walls move apart, and search region initialization from a coarser level plays a similar role.

In this work a multi-level block-matching algorithm is used for motion tracking of carotid plaque images. As with the previously discussed works, displacements tracked at coarser levels are interpolated to initialize the search region location at lower levels. Image sets at every level are created with a scale-space representation of the images [16]. The scale-space representation is chosen because it has many desirable properties including the *non-enhancement* property, i.e. local extrema are not enhanced [16]. If the local extrema are enhanced, artifactual features may be tracked by the similarity metric. Each level in the scale-space is created by filtering the input radio-frequency (RF) image with discrete Gaussian that has a variance $(f/2)^2$ if f is the decimation factor. A three-level image pyramid is created. The decimation factor for each level is given in Table 9.1. Since image content is much denser in the axial direction, higher decimation is allowed in that direction. An example set of scale-space images are shown in Fig. 9.1.

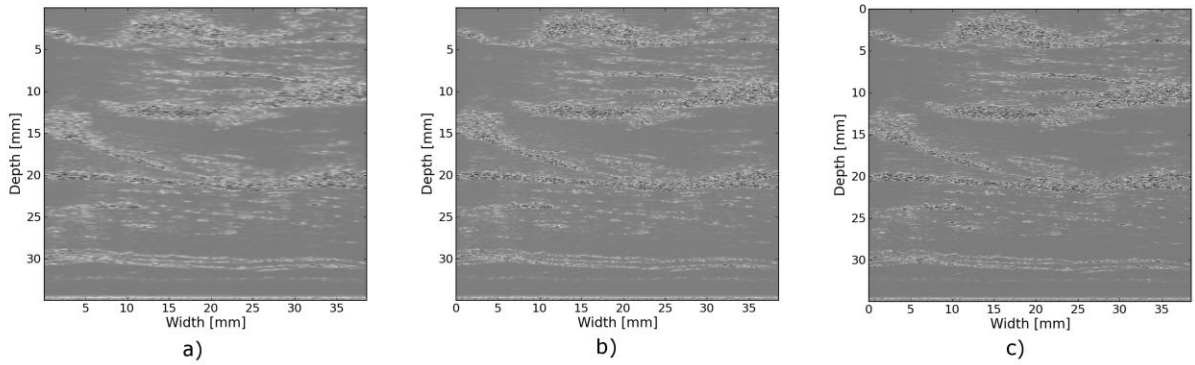

Figure 9.1: Scale-space images for multi-resolution motion tracking. Carotid plaque RF data in the longitudinal view for Subject 157 is shown. The levels, whose decimation factors are given in Table 9.1, are a) level 1, b) level 2, and c) level 3.

Level	Axial decimation factor	Lateral decimation factor
1	3	2

2	2	1
3	1	1

Table 9.1: Downsampling schedule for multi-resolution image registration.

9.1.2 Search region refinement

As previously mentioned, restriction of a matching-block's search region as finer levels in the pyramid are explored can increase the robustness of tracking. For the results explored in this chapter, a simple linear function was applied to reduce the search region size from the coarsest level to the finest level. The value of these parameters is shown in Fig. 9.3. The search region size is expressed as a factor of the matching-block size, and it is greater than 1. Note that even if the search region factor was specified to be the same at the top level and the bottom level, the search region still shrinks in physical size since the matching-block size is specified in pixels and decimation occurs between levels.

While search region restriction can improve robustness, this is not true if there is poor motion tracking in the upper levels. If inaccurate motion tracking occurs at upper levels, the erroneous displacement will propagate to the finer levels. To counter this phenomenon, erroneous displacements are detected and replaced before using them to initialize the center of the search region at lower levels. Peak-hopping errors present themselves as irrationally high strains because they cause a discontinuity in the estimated displacement field. To prevent the propagation of peak-hopping errors, a strain image is generated at the higher levels. Pixels whose strain magnitude exceeds a threshold are marked for replacement. Displacements are then linearly interpolated across a cluster of errant pixels if the pixels are in the center of the image, or they are extrapolated with the slope of the closest good displacement pixels at the edge of the

image. This process is repeated to remove any outliers that remain or were introduced.

9.1.3 Inter-level matching-block scaling

Signal de-correlation within a matching-block is partially caused by the strain within the block [17]. The de-correlation of the matching-block can be reduced by appropriate scaling, 'companding', the matching block by the local strain [18, 19]. In the hierarchical construct, the strain found at higher levels can be used to stretch or compress the matching block before performing cross-correlation at lower levels. This is applied to this algorithm by resampling the matching-block with windowed-sinc interpolation after anisotropically scaling the block by a factor

$$s_i = 1 + e_{ii}^*$$

Eqn. 9.1

where the scaling factor is one plus the normal strain in that direction if the strain is small. Improvement of the strain signal-to-noise ratio (*SNRe*), described in Chapters 3 and 4, for a uniform phantom is demonstrated in Fig. 9.2. There is a significant improvement in the *SNRe* when scaling the matching block. The amount of this improvement increases with the increase in strain magnitude.

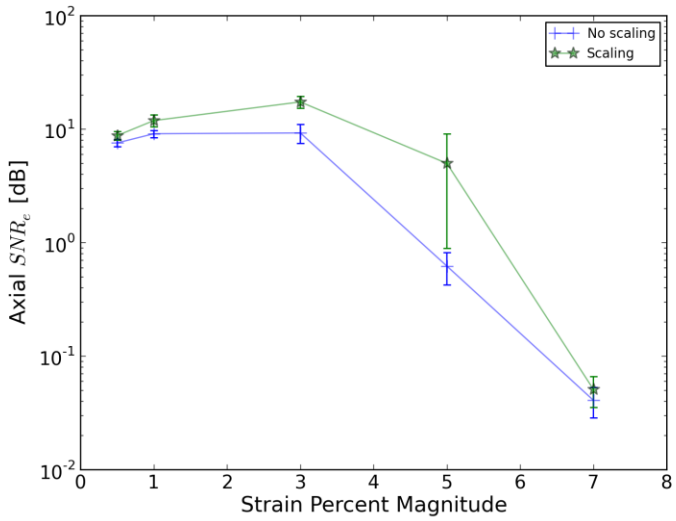

Figure 9.2: Axial strain *SNRe* versus strain magnitude when scaling the matching-block according to the strain obtained in the previous level and without scaling.

9.2 Displacement estimation

Motion tracking is performed with a hierarchical block-matching technique, implemented in C++. A multi-resolution, multi-threaded block-matching framework is implemented on top of the Insight Toolkit [20, 21]. The similarity metric used for comparing a matching-block in the pre-deformation image in its search region in the post-deformation image is normalized cross-correlation. Recursive Bayesian regularization, described in Chapter 3, is used to improve the quality of the tracked displacements at each level. Parabolic interpolation is used to find subsample displacements at the upper levels, and windowed-sinc interpolation with numerical optimization, described in Chapter 4, is used to find subsample displacements at the final level. A central-difference gradient with an order of accuracy of 4, explained in Section 5.2.1, is used to estimate strains at the higher levels where displacement vector sampling is very coarse. Strains at the higher levels are used to remove peak-hopping pixels and to scale the matching-

block in subsequent levels.

Displacements are tracked from a continuous sequence of RF data collected on the longitudinal views of the carotid with the Siemens Antares clinical ultrasound system (Siemens Ultrasound, Mountain View, CA, USA). Patients are scanned prior to a carotid endarterectomy procedure after receiving informed consent on a protocol approved by the University of Wisconsin-Madison Institutional Review Board (IRB). The Siemens Antares VFX13-5 transducer is excited at 11.4 MHz to collect RF at a sampling rate of 40 MHz to a depth of 4 cm. A dynamic frame skip and displacement interpolation algorithm, explained in Section 5.4.1, generates a sequence of incremental displacement images that are evenly spaced in time.

Values of the parameters used in the algorithm are summarized in the configuration file shown in Fig. 9.3. Upsampling on the input two byte signed integer input RF data is performed with windowed-sinc interpolation. The size of the matching-block is specified in samples. To ensure the window is centered on a point, the length of the matching-block is specified as a radius so that the length of the window is $2r + 1$ if r is the radius.

```
# displacement-sequence options input file.
---
files:
  # The input image.   It should be a 3D image where the first two dimensions
  # are space, and the third dimension is time.
  sequenceImage: @SEQUENCE_IMAGE@
  # File name prefix for output files.
  outputPrefix:  @OUTPUT_PREFIX@

parameters:
  # Any point with a strain component above the given value in the higher levels
  # will have its displacement interpolated by surrounding areas.
  maximumAbsStrainAllowed: 0.075
  # Upsampling ratio of the input images.
  upsample: [ 2.0, 2.0 ]
  # Axial direction of the image.
  axialDirection: 1
```

```
  # Related to the matching block.
  block:
    # Block Radius at the top level.
    topBlockRadius:    [ 15, 28 ]
    # Block Radius in at the bottom level.
    bottomBlockRadius: [ 10, 18 ]
    # Block overlap.  1.0 is no overlap.  0.5 is 50% overlap.
    blockOverlap:      1.0
    # In the multiresolution method, scale the matching block by the strain
    # estimated at higher levels.
    scaleByStrain:     true

  # Related to the search region.
  searchRegion:
    # Search region radius at the top level is the following factor times the block
radius.
    # The factors at intermediate levels between the top level and bottom level
    # are linearly interpolated.
    topFactor:     [ 2.2, 1.4 ]
    # Search region radius at the bottom level is the following factor times the block
radius.
    bottomFactor:  [ 1.1, 1.1 ]

  # Related to the Bayesian regularization.
  regularization:
    # Strain regularization parameter.
    strainSigma: [ 0.07, 0.07 ]
    # Maximum number of iterations during regularization at the bottom level.
    maximumIterations: 3

  # Related to the sequential calculation of displacements.
  sequence:
    # The index of the first frame to use as the fixed image.   A value of -1
    # indicates the use of the first index available.   Counts from 0.
    startFrame: @START_FRAME@
    # The index of the last frame to use as the moving image.   A value of -1
    # indicates the use of the last index available.   Counts from 0.
    endFrame:   @END_FRAME@
    # In the case of a static frame skip, this value is the number of frames
    # to between the fixed and moving frame during analysis.   In the case of
    # a dynamic frame skip, i.e.  doDynamicFrameSkip = true, the following
    # value is the maximum number of frames to skip.
    frameSkip:          6
    # Use a dynamic frame skip.   See also 'frameSkip'.   If this value is set
    # to true, the frame skip is varied throughout the sequence by using the
    # strain between the fixed and moving image.
    doDynamicFrameSkip: true
    # In a dynamic frame skip analysis, the maximum absolute strain *in the axial
direction* that should be observed in
```

```
    # a frame skip for best quality.   This value should be the maximum strain
    # that good motion tracking is expected.   The observed maximum strain is
    # smaller than this value, then the frame skip is increased.
    maximumAbsFrameStrain: 0.05
    # In a dynamic frame skip analysis, the percentage of pixels that are
    # allowed over the maximumABSFrameStrain before the frame skip is
    # decreased.
    percentFrameStrainOverMaximumStrain: 2.0
    # We crop the region for the above two strain characteristics to be examined
    # by the following fractional values on both the upper and lower bounds of
    # both directions.
    dynamicStrainCharacteristicsCrop: [ 0.1, 0.30 ]
    # Number of iterations when calculating the inverse displacement for
    # calculating incremental displacements from larger frame skips.
    inverseDeformationIterations: 15
...
```

Figure 9.3: Relevant sections from the algorithm configuration file for motion tracking used to analyze the plaques studied in this chapter.

9.3 Strain estimation

Eulerian incremental frame-to-frame strains at the final level are estimated using the modified least squares estimator described in Section 5.2.3. Prior to strain estimation, the displacements are filtered with a small 3×3 median filter to remove outliers. Parameters of the strain sequence estimation are shown in the configuration file, Fig. 9.4. Note that the output file names contain a reference to the input data they were derived from, a version stamp, and a description of their content. The version stamp is from a source code versioning system (VCS) and is a unique identifier that can be used to obtain the state of the source code when the given results were produced. The input data identifier, source code version, and algorithmic parameters in the configuration file constitute full provenance of the analysis, which ensures repeatability and reproducibility.

```
# strain-sequence options input file.
---
# The file path prefix.   The input is assumed to be
#   <filePrefix>_Version_<version_stamp>_DisplacementVectorSequence.mha
# or
```

```
#   <filePrefix>_Version_<version_stamp>_TrackedMovingFrame*DisplacementVectors.mha
# The output will be
#   <filePrefix>_Version_<version_stamp>_StrainTensorSequence.mha
#   <filePrefix>_Version_<version_stamp>_OrderedPrincipalStrainSequence.mha
#   <filePrefix>_Version_<version_stamp>_EstimatedStrainTensorSequence.mha
#   <filePrefix>_Version_<version_stamp>_EstimatedOrderedPrincipalStrainSequence.mha
# or
#   <filePrefix>_Version_<version_stamp>_TrackedMovingFrame*StrainTensors.mha
#   <filePrefix>_Version_<version_stamp>_TrackedMovingFrame*OrderedPricipalStrains.mha
#   <filePrefix>_Version_<version_stamp>_TrackedMovingFrame*EstimatedStrainTensors.mha
#
<filePrefix>_Version_<version_stamp>_TrackedMovingFrame*EstimatedOrderedPrincipalStrains.m
ha
filePrefix: @FILE_PREFIX@
# The method used to calculate the gradient.   Valid values are "GRADIENT" for a
# numerical gradient calculation or "BSPLINE" for a B-spline approximation
# gradient.  "LEASTSQUARES" for modified linear least squares.
method: LEASTSQUARES
# The ratio of B-spline control points to displacement points.   One value for
# each direction.   This parameter is only relevant when method = BSPLINE.
bSplineControlPointRatio: [1.2, 1.1]
# The radius for performing median filtering on the displacement components.
# Each value with the isotropic radius for the corresponding radius component.
# A value of 0 indicates no median filtering will be applied.
displacementMedianFilterRadius: [1, 1]
# The radius for calculating the linear least squares line fit when calculating
# the displacement gradients.   This parameter is only relevant when method =
# LEASTSQUARES.
leastSquaresStrainRadius: [3, 3]
...
```

Figure 9.4: Configuration file showing the parameters used to calculate incremental strain tensor images from the sequence if incremental tracked displacements.

9.4 Calculation of derived quantities

The final purpose of non-invasive *in vivo* characterization of carotid plaque deformation is to generate a quantity that indicates vulnerability to failure or plaque rupture, thrombogenesis, and ultimately ischemic burden. A number of quantities are derived from the strain tensor over the cardiac cycle as potential indicators of plaque vulnerability. First, regions-of-interest (ROIs) that segment the plaque are created by a radiologist. These ROIs are drawn in a B-Mode image generated from the same RF data used to perform motion tracking. B-Mode and color flow

images taken with clinical imaging features of the scanning system at the time of acquisition are also available to the radiologist to help distinguish atherosclerotic plaque from the lumen and surrounding tissues. Three end-diastolic frames in a dataset are segmented, which delineates two complete cardiac cycles. Contiguous regions are segmented in the image at end-diastole. Often there will be two components corresponding to an anterior and posterior component. However, a highly stenotic plaque may be segmented as a single connected component. Also, due to acoustic shadowing, a plaque may be subdivided into more than two connected components where the echo signal has reasonable amplitudes.

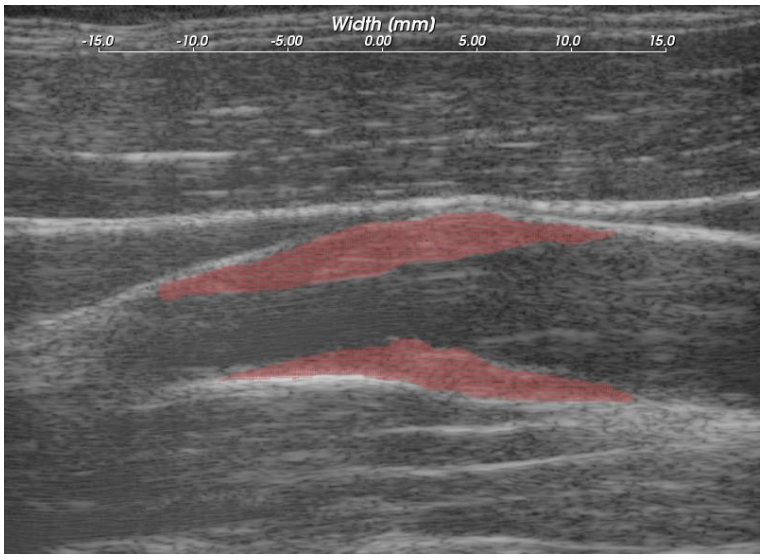

Figure 9.5: Subject 157 ROIs where the particle strains explored in Fig. 9.6 - Fig. 9.9, are tracked over the cardiac cycle.

A binary connected component image is transformed into a mesh. Strains tensors and displacement vectors are accumulated on particles in the mesh as described in Section 5.4.2. Eigen analysis is performed on the accumulated strain tensors to calculate the principal strains, described in Section 5.3.1. The principal strains are used to evaluate the strain metrics: maximum principal strain, maximum shear strain, total strain energy, and distortional energy.

The motivation and definitions of these strain metrics is discussed in Section 5.3.3. To summarize, these metrics define scalars derived from the second-rank tensor that serve as yield criteria, quantities such that if they exceed a threshold, the material will begin to fail. The maximum principal strain suggests that the tissue can only withstand a certain normal strain. Maximum shear strain assumes the material can only withstand a certain shear strain. For a given strain tensor, there is one direction where the maximum normal strain occurs and the maximum shear strain occurs, and the maximum principal and shear strain give the values of these quanities in that direction. Total strain energy and distortional energy yield criteria implying that failure is an energy dependent process. Plaque is a complex material that contains cholesterole, fibrous, calcified, smooth muscle, and hemorrhagic components connected into an amorphous mass. It is also living tissue that dynamically changes its content and connectedness in response to processes like remodeling and inflammation. Therefore, it is difficult to predict *a priori* the yield criteria that best describes the failure process.

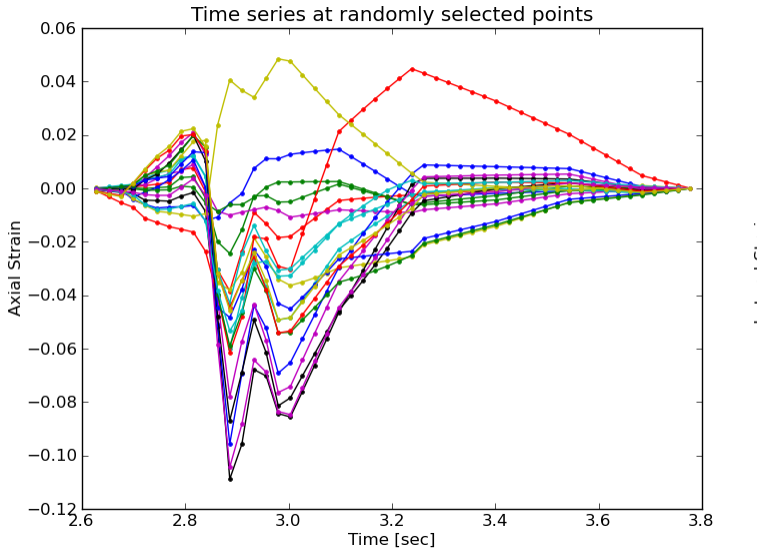

Figure 9.6: Axial strain over the cardiac cycle for 20 randomly selected particles from ROIs highlighted in Fig. 9.5.

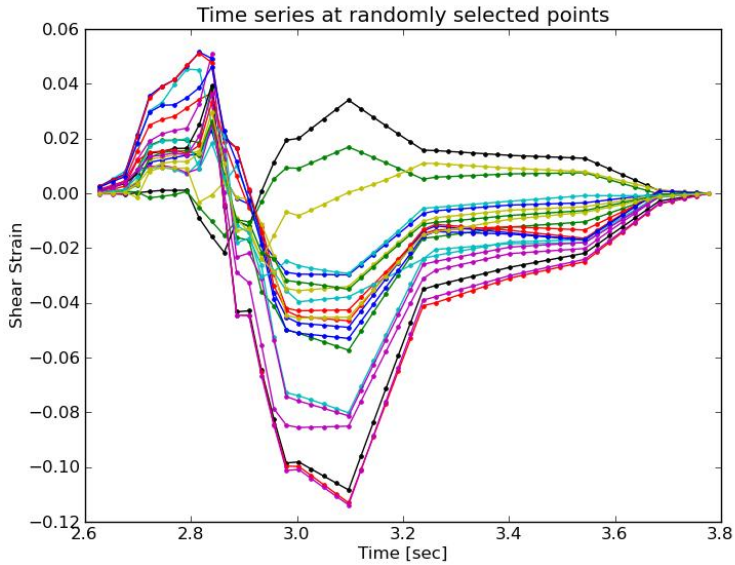

Figure 9.7: Shear strain over the cardiac cycle for 20 randomly selected particles from ROIs highlighted in Fig. 9.5.

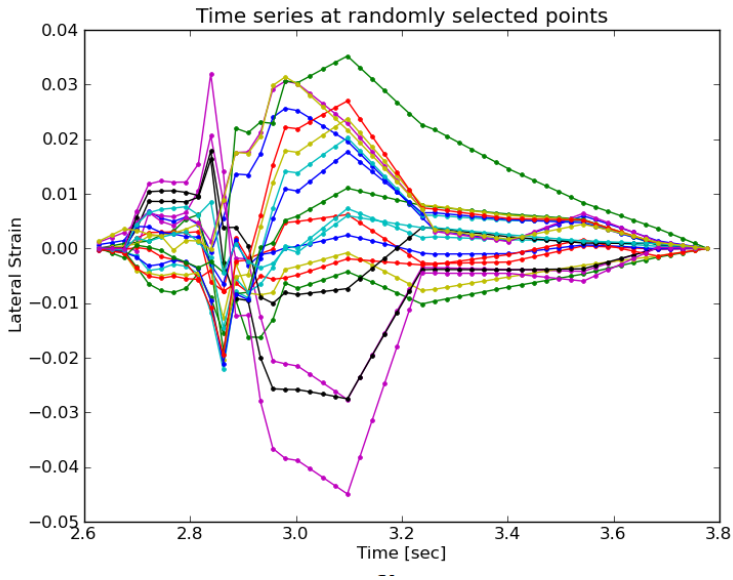

Figure 9.8: Shear strain over the cardiac cycle for 20 randomly selected particles from ROIs highlighted in Fig. 9.5.

Plots of the strain components and strain metrics for Subject 157 are shown in Fig. 9.6 - Fig. 9.9. Twenty randomly selected particles, i.e. mesh points, in the ROIs shown in Fig. 9.5 are

singled out and their accumulated strain values plotted against time. Possibly due to movement in and out of the imaging plane or motion tracking errors, a drift in the accumulated strain is often observed [11]. When there is significant out-of-plane motion, this drift may be explained by the fact that a particle is not accumulating over the same volume of tissue. To compensate for this, the offset at the end of the cycle is linearly removed from every curve. All quantities should start from zero and return to zero if the system is steady-state. While is true in that the tissue obviously remains intact over the examination, some real drift may exist due to breathing, muscle tone, etc.

Recall from Section 5.1.2 that axial strain refers the normal component of the strain tensor along the axis of the ultrasound beam. In this case, Fig. 9.5 and Fig. 9.11, the ultrasound axial direction is to some degree aligned with the radial direction of the vessel. As blood pressure increases, compression is expected in the radial direction [22], which is consistent with the mostly negative strains observed at systole in Fig. 9.6.

In contrast, the shear strains shown in Fig. 9.7 are primarily positive. As indicated by the displacement vectors in Fig. 9.11a), the tissue is consistently sheared from left-to-right in the image, inferior-to-superior in the subject, for both the anterior and posterior ROI. The magnitude of the shear strain is higher than the axial or lateral strains in Fig. 9.6 or Fig. 9.8.

Lateral strains in Fig. 9.8 demonstrate systole and diastole clearly as with the other plots, but do not have a consistent sign. Some strains are positive, which indicates stretching (Chapter 5). The orientation of the plaque and the mechanical loading it experiences does not consistently align with the lateral transducer direction, which explains this variance.

Components of the strain tensor can have positive or negative sign, but all strain metrics should be strictly positive. This is true for all the strain metrics in Fig. 9.9. If this was not true,

strain estimation noise or excessive out-of-plane motion could be suspected. All metrics show a high strain during systole with a slow retraction during diastole. The separation of high strains is accented in the distortional energy plot of Fig. 9.9d) because of squared terms in its expression. The piecewise linear pattern in all plots is attributed to the dynamic frame skip technique, Section 5.4.1. The linearity validates the incremental displacement interpolation algorithm in Section 5.4.1, and the increased duration of the piecewise segments during diastole shows success in the automatic strain assessment method. Some improvements could be made to the automatic strain assessment method to decrease the frame skip slightly at the end of systole here.

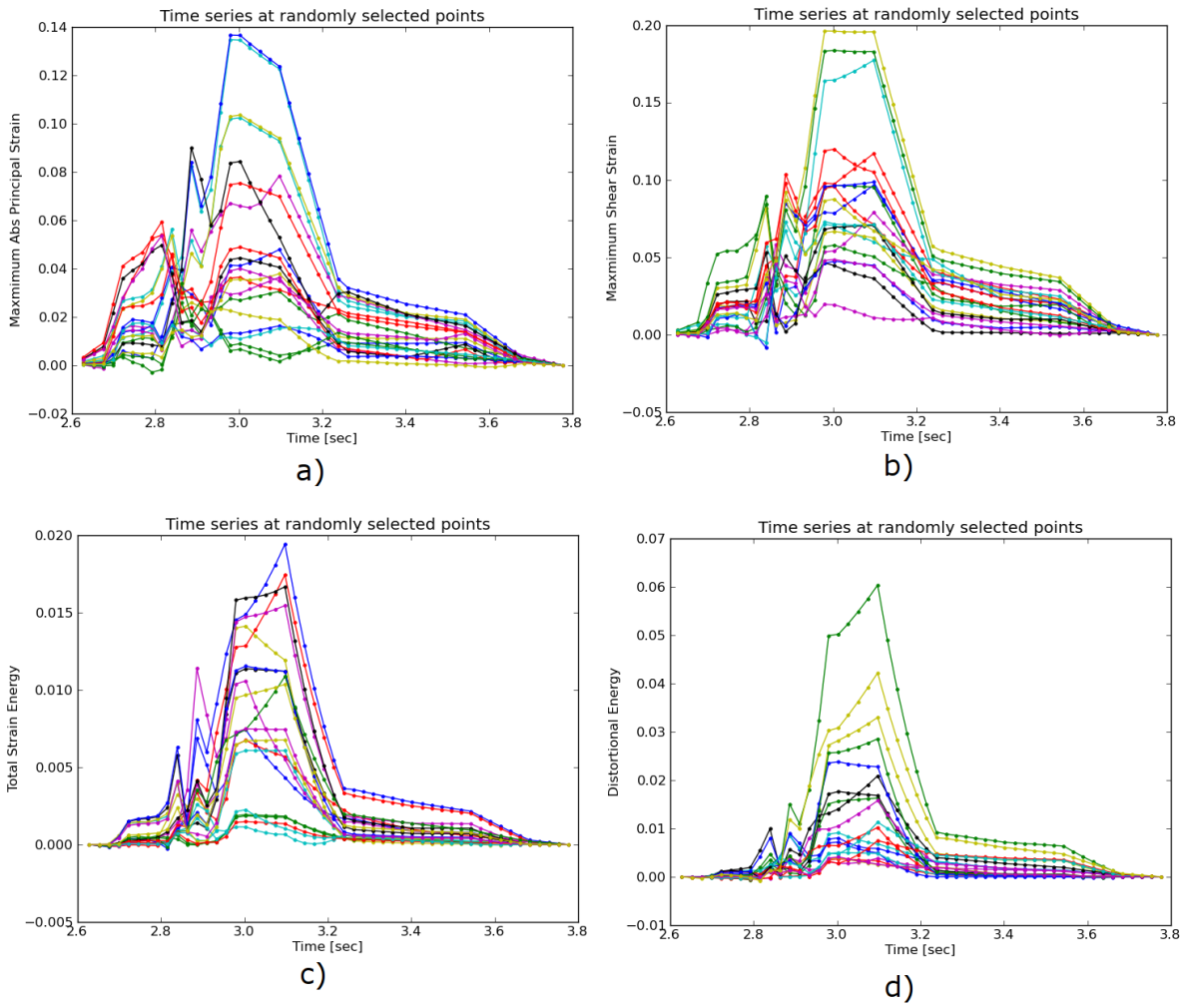

Figure 9.9: Strain metrics over the cardiac cycle for 20 randomly selected particles from ROIs highlighted in Fig. 9.5. a) Maximum principal strain, $max\left\{|\lambda_1|,|\lambda_2|\right\}$, b) maximum shear strain, $\lambda_1-\lambda_2$, c) total strain energy, $\frac{1}{2}E\left(\lambda_1^2+\lambda_2^2\right)$, and d) distortional energy, $\frac{1}{2}E\left(\lambda_1-\lambda_2\right)^2$.

Over the cardiac cycle, the three components of the strain tensor, the maximum principal strain, maximum shear strain, total strain energy, and distortional energy vary over time and over a contiguous region. For each of these values, three scalar statistics are calculated per cardiac cycle. The mean peak-to-peak value reflects the average strain in a region. Since material failure is likely to occur at a location of high strain, the 90th percentile of the peak-to-peak value

is also calculated. A 90th percentile is used instead of the absolute maximum because outliers sometimes arise from part of the ROI crossing into the lumen or movement out-of-plane. Third, the standard deviation of the particle peak-to-peak value is found. This is because strain heterogeneity may mark the presence of highly varying strains beyond the resolution of the system. These three values are found for all strain metrics and strain components. The mean, 90th percentile, and standard deviation of the sum of the magnitude of the time-derivative is also computed. The time-derivative is considered because it is hypothesized that viscoelastic behavior may also contribute to the fatigue failure process. Strain values for five subjects are tabulated in Appendix B.

9.5 *In vivo* case studies

In this section, six *in vivo* plaque case studies are examined that demonstrate different behaviors. These results suggest that strain imaging may measure the end effect of many factors that influence plaque vulnerability: composition (Fig. 9.10), morphology, (Fig. 9.11), hemodynamics (Fig. 9.12), and angiogenesis (Fig. 9.13). Limitations due to acoustic shadowing in Fig. 9.14, and out-of-plane motion in Fig. 9.15, are also illustrated.

9.5.1 Hypoechoic plaque with high strain

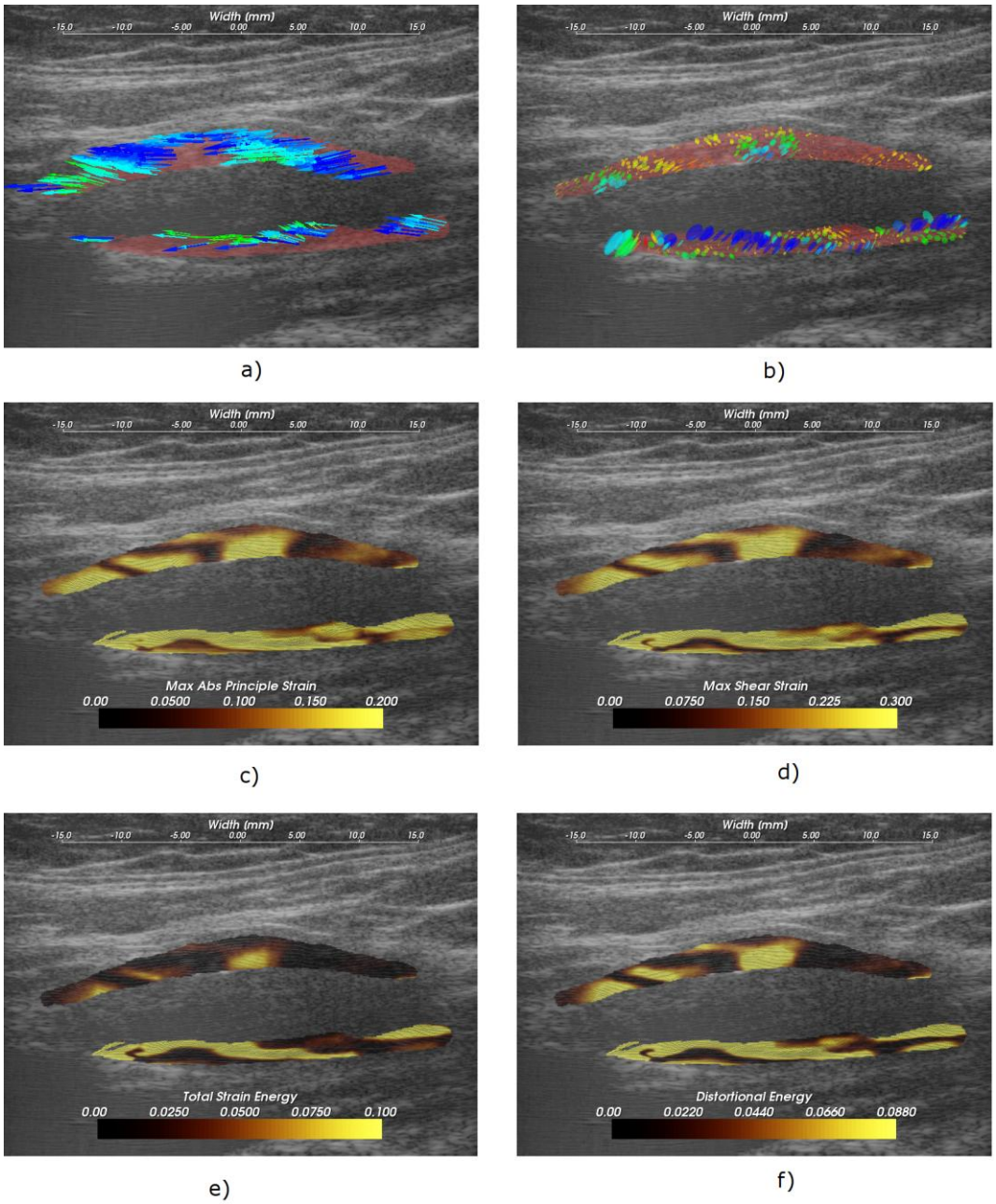

Figure 9.10: A hypoechoic atherosclerotic mass, often classified as 'soft' plaque, that exhibit high strain throughout the plaque. a) Accumulated displacement vectors (movement is primarily in superior direction), b) strain tensor ellipses, c) maximum absolute principal strain, d) maximum shear strain, e) total strain energy, and f) distortional energy.

As discussed in Section 2.3.1, hypo-echoic B-Mode presentation is associated with lipid or hemorrhagic plaque content. It has traditionally been hypothesized that soft plaques may be a

sign of vulnerability. In Fig. 9.10, a hypoechoic plaque from the right side of Subject 154 is shown to have high strains throughout the plaque. Strain in the posterior plaque segment (found deeper in the image), is higher than the anterior plaque segment. This pattern is common, and could be related to material properties of the tissue surrounding the anterior segment compared to the material properties surrounding the posterior segment, or it could be related to the compression supplied by the transducer [23]. The mean peak-to-peak maximum absolute principal strain is 0.23 and the 90th percentile is 0.41 in the posterior segment (Table B.1). There is little difference in the distribution of the strain metrics in this case with the possible exception of the total strain energy, which is more reserved in the anterior segment. These strain tensor ellipses allow easy comprehension of the magnitude, orientation, and distribution of the strain. The changing orientation of the ellipses explain the contours of low strain metric amplitude in Fig. 9.10c)-f); low strain metric amplitude occurs as transitions in the orientation of deformation. Displacements illustrated in Fig. 9.10a) are large and predominantly lateral, which underscores the need for good lateral tracking.

9.5.2 Importance of morphology

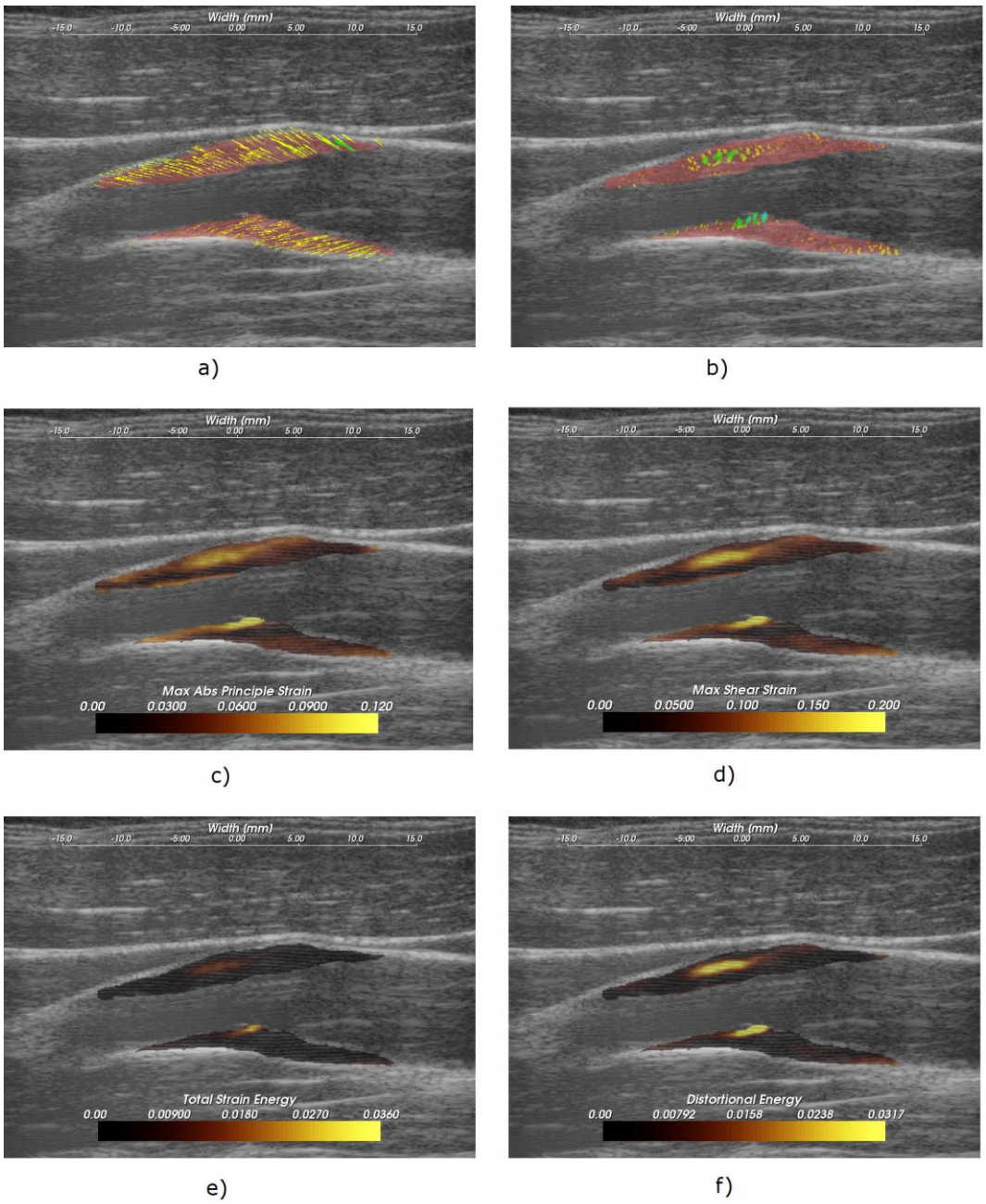

Figure 9.11: Strain pattern in an echogenically homogeneous plaque that varies depending on the geometry of the plaque and its position relative to blood flow. a) Displacement vectors, b) strain tensor ellipses, c) maximum absolute principal strain, d) maximum shear strain, e) total strain energy, and f) distortional energy.

As discussed in Section 2.2 and 2.3, the dominant focus of various imaging and other

diagnostic techniques is on identification of plaque composition. While composition may be an important factor in plaque vulnerability, it is not the only factor. In Fig. 9.11, a plaque with a relatively homogeneous B-Mode echogenicity is shown, which implies that its composition may be homogeneous. However, when mechanical loading is applied via the pulse pressure, a heterogeneous strain distribution results. Strain is highest in the center of the larger anterior plaque region and falls off towards its edges. The area of the posterior plaque segment that protrudes into the lumen experiences much higher strain than other areas.

Subtle but significant differences in the strain metrics shown in Fig. 9.11c)-f) are apparent. The squared terms in the total strain energy and distortional energy accentuate the locations of highest strain compared to the maximum absolute principal strain and the maximum shear strain. These images are from the left side of Subject 157.

9.5.3 Strain with turbulent flow

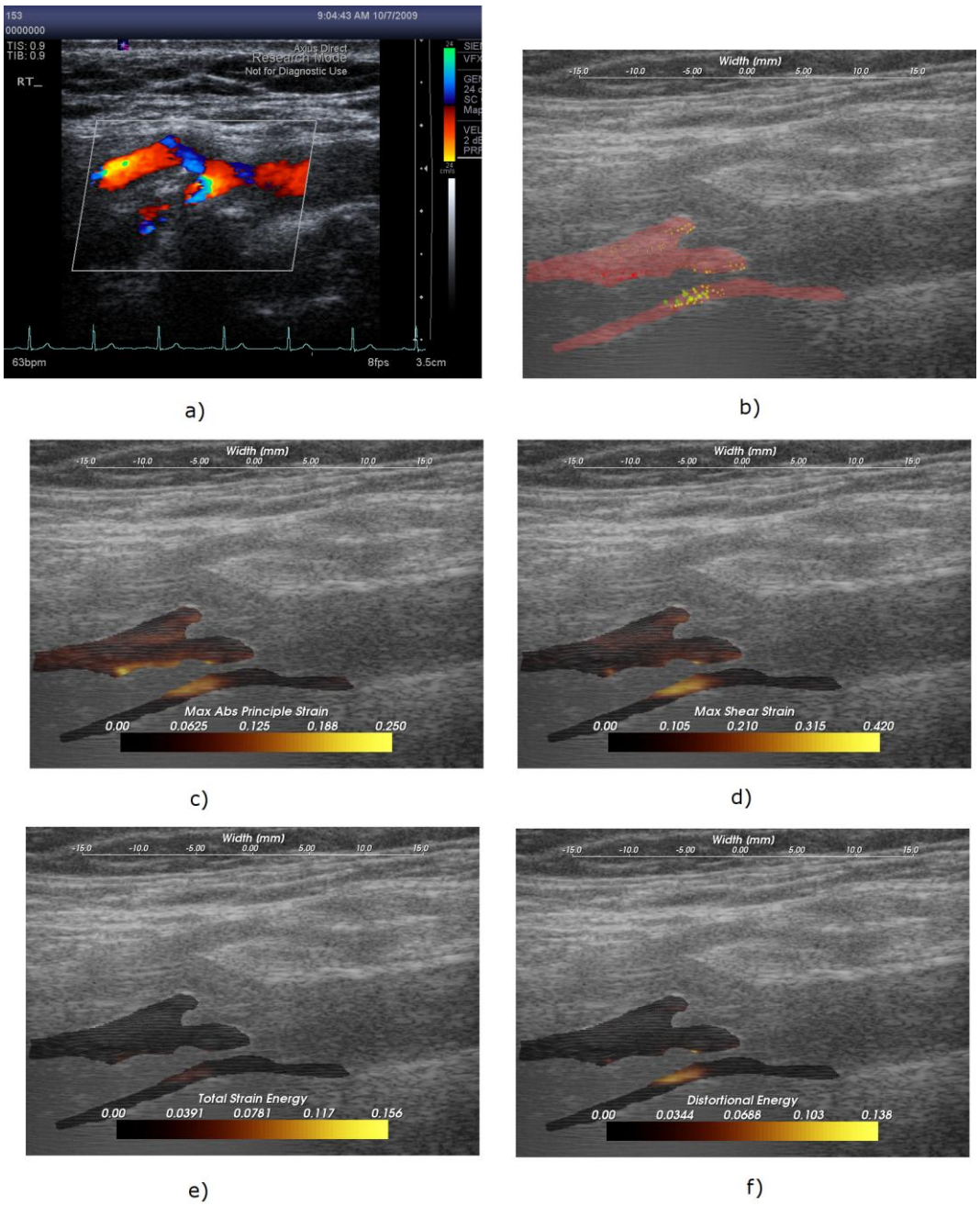

Figure 9.12: High strain adjacent to turbulent flow that follows a narrow inlet in the ICA. a) Color flow from the scanner interface, b) strain tensor ellipses, c) maximum absolute principal strain, d) maximum shear strain, e) total strain energy, and f) distortional energy.

Figure 9.11 emphasizes that morphology is an important factor in plaque vulnerability, and strain imaging captures that factor. The material composition does not independently predict

plaque vulnerability as commonly assumed, but the importance of a necrotic core, for example depends on its location within the mechanical environment [24]. Figure 9.12 suggests that hemodynamics are also a factor in plaque vulnerability. Aliasing in the color flow image, shown in Fig. 9.12a), can be attributed to the turbulent flow that occurs as the blood squeezes through the small patency in the plaque at the base of the internal carotid artery (ICA). High strain is seen in the plaque immediately adjacent to this location of turbulent flow.

9.5.4 Strain at the plaque-adventitia interface

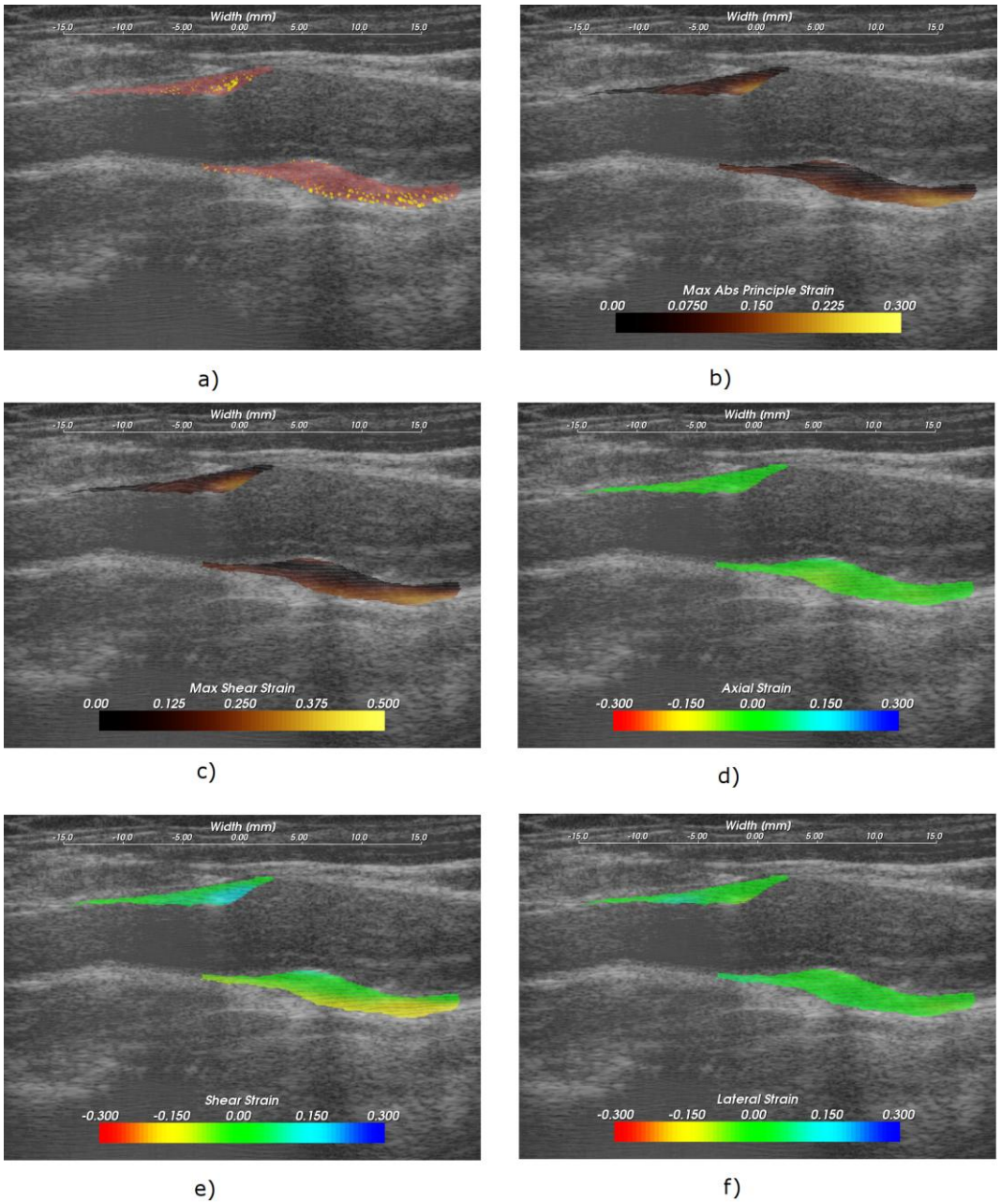

Figure 9.13: High strain near the interface of the plaque with the surrounding tissue that occurs with lateral motion of the plaque. a) Strain tensor ellipses, b) maximum absolute principal strain, c) maximum shear strain, d) axial strain, e) shear strain, f) and lateral strain.

Recall that angiogenesis has also been proposed in the literature as a possible factor leading to plaque vulnerability [25, 26, 27, 28]. As plaques become larger, the vasa vasorum that

provided blood to the artery wall can grow to feed the enlarged tissue. These fissures are expected to cause instability associated with the adventitia-plaque boundary where angiogenesis originates. Figure 9.13 shows high strains at this location occurring during lateral motion of the plaque that may be associated with this phenomenon. These images are from the left side of Subject 156.

Examining the strain tensor ellipses or the strain metric images, we easily locate the areas of high strain. A single component of the strain tensor does not always provide sufficient information. In this case, for example, the high strain is not apparent in the axial or lateral strain images. Note that the ellipses are orientated at an angle of $3\pi/4$ because of the orientation and deformation of the plaque. This off-axis orientation explains why the strain is best reflected in the shear strain component in this case. If the plaque was orientated in a more horizontal direction relative to the transducer, the strain would then arise in the lateral component.

Again, note that the area of the anterior plaque that protrudes into the lumen is subject to high strains.

9.5.5 Calcified plaque with shadowing

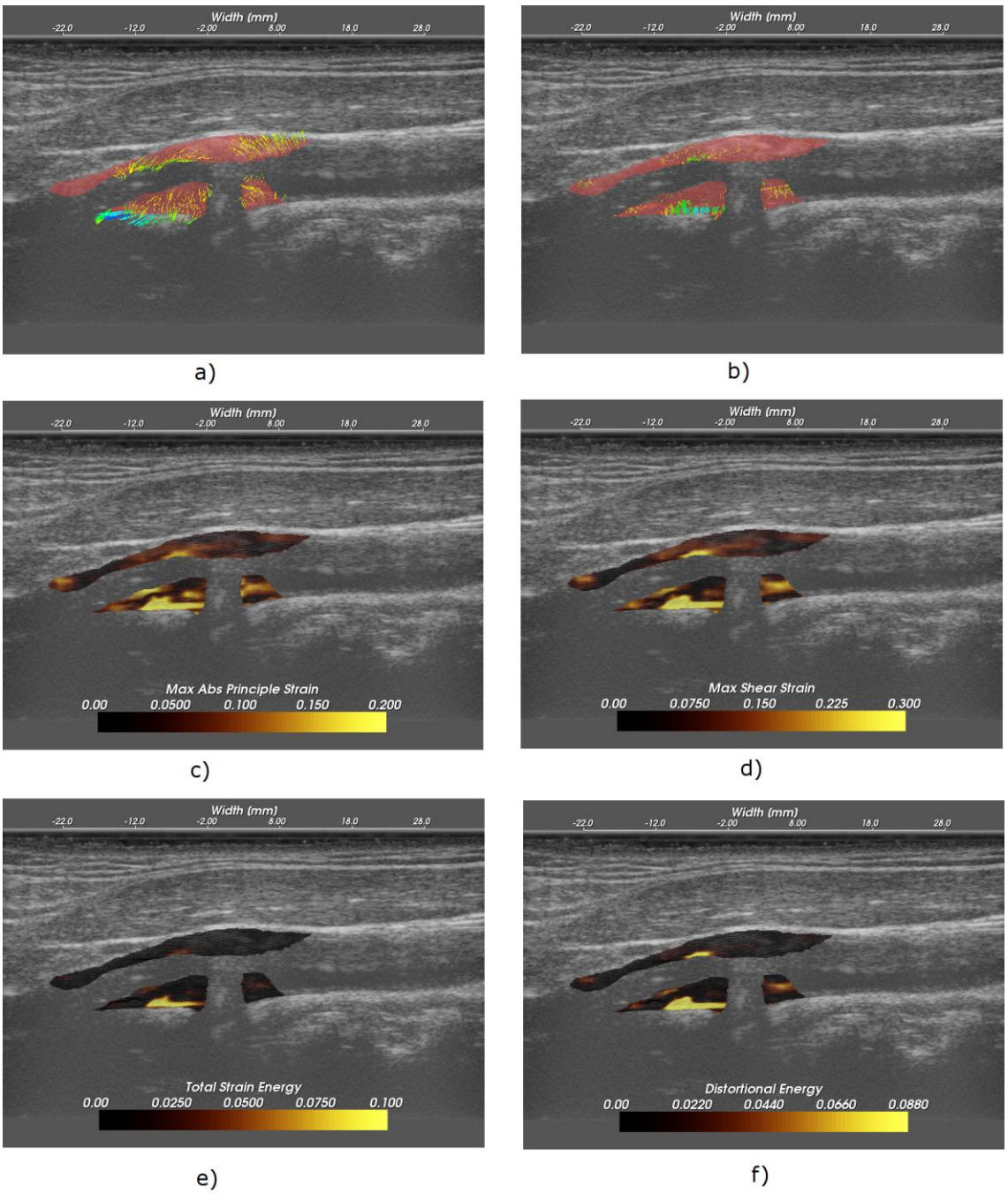

Figure 9.14: Low strain in a calcified plaque, but high strain in other areas. a) Displacement vectors, b) strain tensor ellipses, c) maximum absolute principal strain, d) maximum shear strain, e) total strain energy, and f) distortional energy.

It is well known that calcified plaques are associated with high acoustic attenuation and that

they are extremely stiff. The increased attenuation explains the acoustic shadowing on these images of the left side of Subject 158. As the displacement vectors indicate in Fig. 9.14a), this plaque undergoes a torsional motion when subject to the pressure pulse. Very little strain occurs in the highly calcified region that causes the shadowing. In other areas of the plaque that appear to have heterogeneous calcification, very high strains occur. Examination of the strain time series suggests that this may result from a combination of heterogeneous calcification, morphology, and hemodynamics.

This case also illustrates a limitation of non-invasive externally applied ultrasound imaging. Motion tracking cannot be performed when calcified plaques attenuate the ultrasound beam to undetectable levels. Furthermore, the 2D imaging method can only capture a small subset of the imaging planes available. For a heterogeneous structure like carotid plaques, a critical region may be overlooked. Additionally, not all components of the 3D strain tensor are captured. Strain imaging in the transverse plaque is made more difficult by the motion pattern that occurs in this direction and refraction of the beam by the artery wall [29, 30].

9.5.6 Artifact from out-of-plane motion

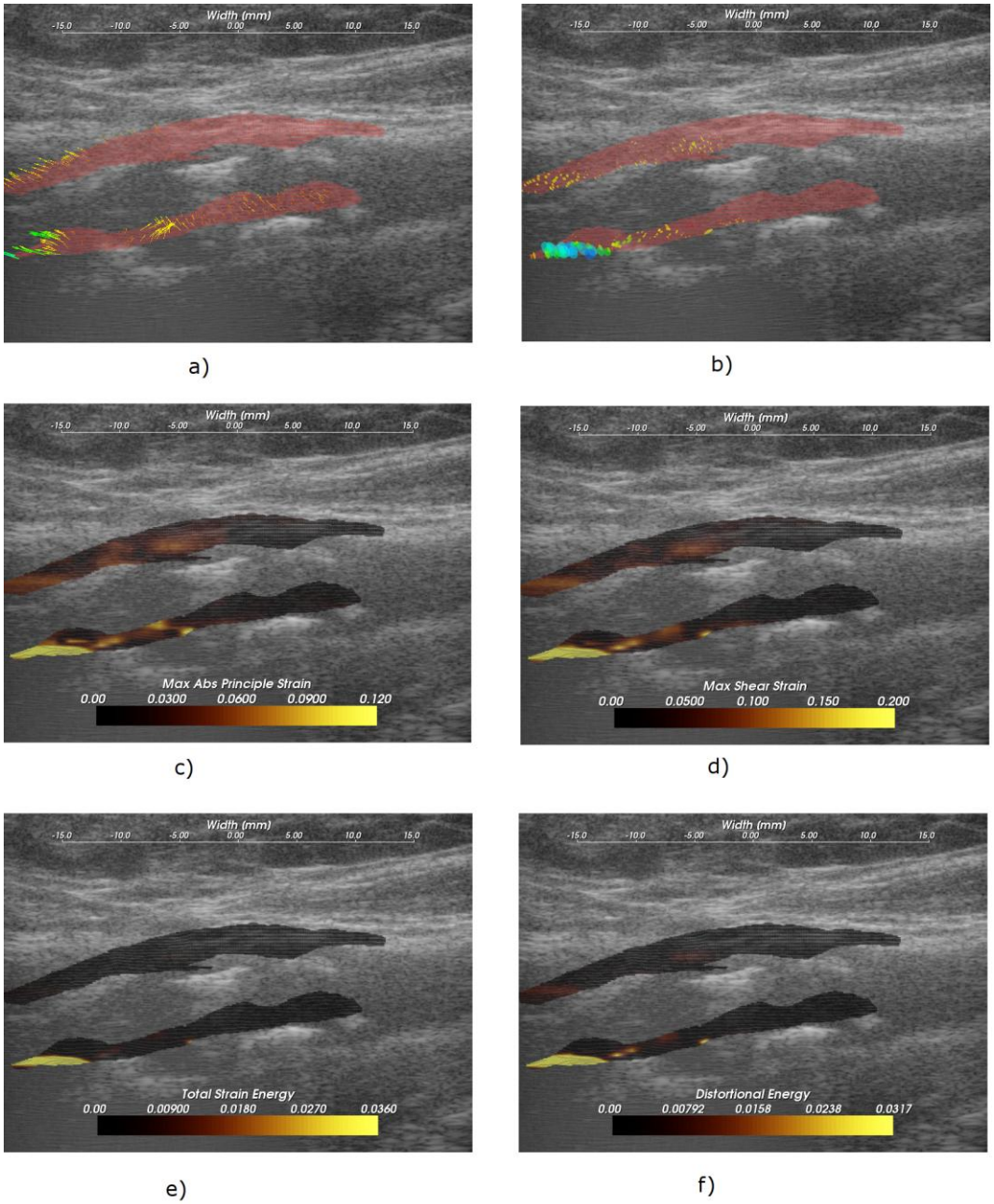

Figure 9.15: High accumulated strain artifacts attributable to out-of-plane motion. a) Displacement vectors, b) strain tensor ellipses, c) maximum absolute principal strain, d) maximum shear strain, e) total strain energy, and f) distortional energy.

Finally, a case where artifactual high strains occur with data from the left side of Subject 153 is displayed in Fig. 9.15. At the edge of ROIs such as this one, the vessel is twisting away

from the plane of the transducer. This has multiple negative effects. Out-of-plane motion is increased, which causes signal decorrelation and increases strain image noise. Out-of-plane motion also means a particle does not track the same volume of tissue over time. Furthermore, orientation of the principal axes of the strains accumulated may differ, which will not result in the correct accumulation of the strain tensor.

9.6 References

[1] Y. Wu, L. Chen, P. Lee, T. Yeh and J. Hsieh. Discrete signal matching using coarse-to-fine wavelet basis functions. *Pattern Recognition* 36, 171--192. 2003.

[2] B. Likar, F. Pernus and A. Hierarchical Approach to Elastic Registration Based on Mutual Information. *information, Image and Vision Computing* 19, 33--44. 2001.

[3] Y. Wu, T. Kanade and J. Cohn. Image Registration Using Wavelet-Based Motion Model. *International Journal of Computer Vision* 38, 129--152. 2000.

[4] W. R. Crum. Non-rigid image registration: theory and practice. *British Journal of Radiology* 77, S140--S153. 2004.

[5] D. Tzovaras. Evaluation of multiresolution block matching techniques for motion and disparity estimation. *Signal Processing: Image Communication* 6, 59--67. 1994.

[6] J. A. Schnabel, D. Rueckert, M. Quist, J. M. Blackall, A. D. Castellano-smith, T. Hartkens, G. P. Penney, W. A. Hall, H. Liu, C. L. Truwit, F. A. Gerritsen, D. L. G. Hill and D. J. Hawkes. A Generic Framework for Non-rigid Registration Based on Non-uniform Multi-level Free-Form Deformations. *MICCAI* 2208, 573--581. 2001.

[7] B. C. Vemuri, S. Huang, S. Sahni, C. M. Leonard, C. Mohr, R. Gilmore and J. Fitzsimmons. An efficient motion estimator with application to medical image registration.. *Medical Image Analysis* 2, 79--98. 1998.

[8] B. Zitova. Image registration methods: a survey. *Image and Vision Computing* 21, 977--1000. 2003.

[9] F. Yeung, S. F. Levinson and K. J. Parker. Multilevel and motion model-based ultrasonic speckle tracking algorithms. *Ultrasound in Medicine & Biology* 24, 427--442. 1998.

[10] C. Pellot-Barakat, F. Frouin, M. F. Insana and A. Herment. Ultrasound elastography based on multiscale estimations of regularized displacement fields. *IEEE Transactions on Medical Imaging* 23, 153--63. 2004.

[11] H. Shi and T. Varghese. Two-dimensional multi-level strain estimation for discontinuous tissue. *Physics in Medicine and Biology* 52, 389--401. 2007.

[12] J. Bai, C. Ding and Y. U. Fan. A multi-scale algorithm for ultrasonic strain reconstruction under moderate compression. *Ultrasonics* 37, 511--519. 1999.

[13] A. Basarab, H. Liebgott, F. Morestin, A. Lyshchik, T. Higashi, R. Asato and P. Delachartre. A method for vector displacement estimation with ultrasound imaging and its application for thyroid nodular disease. *Medical Image Analysis* 12, 259--74. 2008.

[14] L. Chen, R. J. Housden, G. M. Treece, A. H. Gee, R. W. Prager and T. Street. A hybrid displacement estimation method for ultrasonic elasticity imaging. *IEEE Transactions on Ultrasonics, Ferroelectrics and Frequency Control* 57, 866--882. 2010.

[15] J. Jiang and T. J. Hall. A Generalized Speckle Tracking Algorithm for Ultrasonic Strain Imaging Using Dynamic Programming. *Ultrasound in Medicine & Biology* 35, 1863--1879. 2009.

[16] T. Lindeberg. *Scale-Space Theory in Computer Vision*. : Springer. 1994.

[17] T. Varghese, J. Ophir and I. Cespedes. Noise reduction in elastograms using temporal stretching with multicompression averaging. *Ultrasound in Medicine & Biology* 22, 1043--1052. 1996.

[18] P. Chaturvedi, M. F. Insana and T. J. Hall. 2D companding for noise reduction in strain imaging. *IEEE Transactions on Ultrasonics, Ferroelectrics, and Frequency Control* 45, 179--191. 1998.

[19] P. Chaturvedi, M. F. Insana and T. J. Hall. Testing the limitations of 2-D companding for strain imaging using phantoms. *IEEE Transactions on Ultrasonics, Ferroelectrics, and Frequency Control* 45, 1022--31. 1998.

[20] L. Ibanez, W. Schroeder, L. Ng and J. Cates. The ITK Software Guide. 2005.

[21] T. S. Yoo, M. J. Ackerman, W. E. Lorensen, W. Schroeder, V. Chalana, S. Aylward, D. Metaxes and R. Whitaker. "Engineering and Algorithm Design for an Image Processing API: A Technical Report on ITK - The Insight Toolkit". In Westwood, J. (Eds.) *Medicine Meets Virtual Reality*, Amsterdam: IOS Press. 2002.

[22] H. H. G. Hansen, R. G. P. Lopata, T. Idzenga and C. L. de Korte. Full 2D displacement vector and strain tensor estimation for superficial tissue using beam-steered ultrasound imaging. *Physics in Medicine and Biology* 55, 3201--18. 2010.

[23] R. L. Maurice, G. Soulez, M. Giroux and G. Cloutier. Noninvasive vascular elastography for carotid artery characterization on subjects without previous history of atherosclerosis. *Medical Physics* 35, 3436. 2008.

[24] G. C. Makris and Nicolaides. Introduction to the biomechanics of carotid plaque pathogenesis and rupture: review of the clinical evidence. *The British Journal of Radiology* 83, 729--35. 2010.

[25] M. J. McCarthy, I. M. Loftus, M. M. Thompson, L. Jones, N. J. M. London, P. R. F. Bell, A. R. Naylor and N. P. J. Brindle. Angiogenesis and the atherosclerotic carotid plaque: an association between symptomatology and plaque morphology. *Journal of Vascular Surgery* 30, 261--268. 1999.

[26] R. J. Lusby, L. D. Ferrell, W. K. Ehrenfeld, R. J. Stoney and E. J. Wylie. Carotid plaque hemorrhage. Its role in production of cerebral ischemia. *Arch Surg* 117, 1479--1488. 1982.

[27] T. Hiyama, T. Tanaka, S. Endo, K. Komine, T. Kudo, H. Kobayashi and Y. Shiokawa. Angiogenesis in Atherosclerotic Plaque Obtained From Carotid Endarterectomy: Association Between Symptomatology and Plaque Morphology. *Neurologia medico-chirurgica* 50, 1056--1061. 2010.

[28] E. Vicenzini, M. F. Giannoni, F. Puccinelli, M. C. Ricciardi, M. Altieri, V. Di Piero, B. Gossetti, F. B. Valentini and G. L. Lenzi. Detection of carotid adventitial vasa vasorum and plaque vascularization with ultrasound cadence contrast pulse sequencing technique and echo-contrast agent. *Stroke* 38, 2841--3. 2007.

[29] H. H. G. Hansen, R. G. P. Lopata and C. L. de Korte. Noninvasive carotid strain imaging using angular compounding at large beam steered angles: validation in vessel phantoms.

IEEE Transactions on Medical Imaging 28, 872--80. 2009.

[30] H. H. G. Hansen, R. G. P. Lopata, T. Idzenga and C. L. de Korte. Full 2D displacement vector and strain tensor estimation for superficial tissue using beam-steered ultrasound imaging. *Physics in Medicine and Biology* 55, 3201--18. 2010.